Article

Two-Dimensional $Cs_3Sb_2I_{9-x}Cl_x$ Film with (201) Preferred Orientation for Efficient Perovskite Solar Cells

Jihong Li [1,2], Yongao Lv [1,2], Huifang Han [1,2], Jia Xu [1,2] and Jianxi Yao [1,2,*]

[1] State Key Laboratory of Alternate Electrical Power System with Renewable Energy Sources, North China Electric Power University, Beijing 102206, China; lijihong2413@gmail.com (J.L.); lvyongao@163.com (Y.L.); huifanghan@ncepu.edu.cn (H.H.); xujia@ncepu.edu.cn (J.X.)

[2] Beijing Key Laboratory of Energy Safety and Clean Utilization, North China Electric Power University, Beijing 102206, China

[*] Correspondence: jianxiyao@ncepu.edu.cn

Abstract: All-inorganic Sb-perovskite has become a promising material for solar cell applications owing to its air stability and nontoxic lead-free constitution. However, the poor morphology and unexpected (001) orientation of Sb-based perovskite films strongly hinder the improvement of efficiency. In this work, two-dimensional $Cs_3Sb_2Cl_xI_{9-x}$ with (201) preferred orientation has been successfully fabricated by introducing thiourea (TU) to the precursor solution. The presence of the C=S functional group in TU regulates the crystallization dynamics of $Cs_3Sb_2I_{9-x}Cl_x$ films and generates the (201) preferred orientation of $Cs_3Sb_2Cl_xI_{9-x}$ films, which could effectively improve the carrier transport and film morphology. As a result, the $Cs_3Sb_2I_{9-x}Cl_x$ perovskite solar cells (PSCs) delivered a power conversion efficiency (PCE) of 2.22%. Moreover, after being stored in nitrogen at room temperature for 60 days, the devices retained above 87.69% of their original efficiency. This work demonstrates a potential pathway to achieve high-efficiency Sb-based PSCs.

Keywords: lead-free; Sb-perovskite; $Cs_3Sb_2I_{9-x}Cl_x$; solar cells

1. Introduction

The power conversion efficiency (PCE) of perovskite solar cells (PSCs) has achieved 25.7% owing to the optimal optoelectronic performance [1]. However, the toxicity of water-soluble lead remains a major deterrent to the application of Pb-based PSCs, posing a threat to soil and underground water resources. [2]. Therefore, several environmentally friendly elements (Sn, Bi) have been used to replace Pb [3,4]. So far, Sn-PSCs, Sb-PSCs, and Bi-PSCs have demonstrated the highest PCEs of 14.6%, 3.43%, and 3.2%, respectively [5–7]. Nevertheless, the main issue is that the Sn-based perovskite is liable to oxidize to Sn^{4+} in air or an inert environment [8].

Recently, all-inorganic $Cs_3Sb_2I_9$ perovskites have also attracted significant interest because of their high absorption coefficient ($>10^5$ cm^{-1}) and excellent moisture and thermal stability [9–11]. In general, two main crystal structures exist for $Cs_3Sb_2I_9$, namely, the zero-dimensional (dimer) and two-dimensional (layered) phases [12]. The 0 D phase has inherent problems, including poor carrier transport and an indirect bandgap greater than 2.2 eV, which are detrimental to the PCE [13]. Jiang et al. proved in theory and practice that replacing iodide with chloride in the $Cs_3Sb_2I_9$ lattice can effectively suppress the formation of undesirable 0 D phases [9]. Peng et al. also reported that the replacement of a fraction of iodine with chlorine could obtain high-quality 2D $Cs_3Sb_2Cl_xI_{9-x}$ films with a PCE of 2.15% [14]. Umar et al. fabricated 2D $Cs_3Sb_2I_9$ via a HCl-assisted solution method, but the rapid crystallization rate produced smaller grain sizes (~50 nm), limiting the efficiency to 1.21% [13]. To decrease the rate of perovskite crystallization and increase the grain size, N-Methyl-2-pyrrolidone (NMP), thiourea (TU), and bis (trifluoromethane) sulfonimide lithium (LiTFSI) have been adopted as an additive to form complexes with Sb^{3+}, which

could retard the perovskite formation process through an intramolecular exchange [7,15,16]. Generally, the preferential (001) plane of $Cs_3Sb_2I_9$ is parallel to the substrate, which is a big obstacle preventing the improvement of the device performance. As we know, it is expected that the perovskite crystal grows vertical to the electrodes to enable an efficient charge transport up and down [17].

Therefore, modulation of the $Cs_3Sb_2I_9$ crystal orientation to facilitate carrier transport was an issue of concern for $Cs_3Sb_2I_9$ solar cells. Singh et al. found that introducing the coordination molecule indacenodithiophene-based organic acceptor (ITIC) into $Cs_3Sb_2I_9$ films could effectively enhance the (201) orientation and achieve a PCE of 3.25% [10]. According to these studies, either Cl^- or coordination molecules could improve the crystallization of Sb-based perovskite and enhance the photovoltaic performance.

In this work, high quality $Cs_3Sb_2I_{9-x}Cl_x$ films with the preferential orientation of the (201) plane have been successfully fabricated by introducing TU to regulate perovskite crystallization. It was determined that the C=S group in TU can combine with Sb^{3+} to form a complex in the perovskite precursor, which significantly retards the crystallization. X-ray photoelectron spectra (XPS) verified that the TU could be eventually removed from the films, which had no effect on the component of the perovskite films. Based on the density functional theory (DFT) calculations, TU has a much lower adsorption energy (-0.22 eV) on the perovskite (003) crystalline plane than it does on the (201) plane (-0.36 eV). The perovskite (003) crystalline plane with a lower adsorption energy grows much more quickly than the (201) crystalline plane. In accordance with the Bravais–Riedel–Donnay–Harker laws, there is a tendency for crystalline planes growing quickly to decrease or even vanish [18]. As a result, high-quality $Cs_3Sb_2I_{9-x}Cl_x$ films with the (201) preferential orientation and a large grain size have been successfully obtained by optimizing the amount of TU in the precursors. The PCE has been promoted to 2.22%, with a notable multiplied J_{SC} of 6.77 mA cm^{-2}, V_{OC} of 0.65 V, and FF of 50.3%. Moreover, the devices retained 87.69% of its initial efficiency after being stored in a nitrogen environment at room temperature for 60 days.

2. Experimental

2.1. Materials

SbI_3 (98% metals basis, Sigma–Aldrich, St. Louis, MO, USA), $SbCl_3$ (Sigma–Aldrich, St. Louis, MO, USA), Bis-(trifluoromethane) sulfonimide lithium salt (Xi'an Polymer Light Technology Corp, Xi'an, China), Thiourea (TU) (Sigma–Aldrich, St. Louis, MO, USA), tert-butylpyridine (tBP) (Xi'an Polymer Light Technology Corp, Xi'an, China), CsI (Xi'an Polymer Light Technology Corp, Xi'an, China), spiro-OMeTAD (99.7% Borun Chemicals, Zhejiang, China), DMF (Alfa-Aesar, Ward Hill, MA, USA), Isopropanol (J&K Scientific Co., Ltd., Beijing, China), and FK209-cobalt (III)-TFSI (MaterWinChemicals, Shanghai, China) were used as received.

2.2. Device Fabrication

The FTO substrates were cleaned with deionized water and ethanol for 20 min in an ultrasonic bath and then a UV–ozone treatment was performed for 30 min. The compact TiO_2 and mp–TiO_2 layers were deposited according to our previous method [19]. The precursor solution was prepared by dissolving 1 M CsI, 0.23 M $SbCl_3$, and 0.02 M SbI_3 in a 1 mL mixed of DMSO and DMF (3:1, *v/v*) and stirred at 70 °C for 12 h. Then the solution was spin–coated on FTO/c–TiO_2/mp–TiO_2 substrates at 3000 rpm for 30 s. After spin coating, the films annealed at 70 °C for 10 min to remove the solvents, followed by a SbI_3 vapour annealing at 250 °C for 15 min. The SbI_3 vapour was prepared by a 30 wt% SbI_3 DMF solution (5 μL) dropping to the corner of the petri dish during annealing. For the TU additive sample, the desired amount of TU was added into the precursor and the above-mentioned film-formation protocol was followed. After that, the hole transporting layer and electrode were deposited according to our previous method [19].

2.3. Device Characterization

UV–vis spectra were acquired with the UV–2450 (Shimadzu, Kyoto, Japan) from 400 nm to 900 nm. XRD patterns were obtained via an X-ray diffractometer (XRD, Smart-Lab, Rigaku, Tokyo, Japan) with Cu–Kα radiation (1.5418) (5°–55°, 4° min^{-1}). The morphologies and roughness were measured with the SU8010 SEM (Hitachi, Chiyoda City, Japan, 3.0 kV, 10100 nA) and 5500 AFM (Agilent Technologies, Santa Clara, CA, USA), respectively. Steady–state photoluminescence (PL) spectra were collected with a Fluorolog–322 (Horiba, Edison, NJ, USA). Time-resolved photoluminescence (TRPL) spectra were measured with the FLS1000 (Edinburgh Instruments, Livingston, UK). The FTIR spectrum was acquired with the Excalibur 3100 (Varian, Palo Alto, CA, USA). X–ray spectra (XPS) were acquired with the ESCALab250Xi, Thermo Fisher Scientific, Waltham, MA, USA. Impedance spectroscopy was measured via a Zahner electrochemical workstation (Zahner, Kronach, Germany) with a bias potential of 0.50 V in the dark with the frequency ranging from 100 Hz to 1 MHz. The *J–V* curves were tested via a Keithley 2400 source-meter under AM 1.5G 100 mW cm^{-2} from a sunlight simulator (XES–300T1, SAN–EI Electric, Tokyo, Japan). The capacitance-voltage (C–V) measurements was performed using a Zahner electrochemical workstation in the dark at a frequency of 10 kHz and the AC amplitude was 10 mV. The incident photon–to–electron conversion efficiency (IPCE) was recorded by a QE-R measurement system (Enli Technology, Kaohsiung City, Taiwan).

2.4. DFT Calculations

The first–principles calculations were done with VASP (Vienna Ab–initio Simulation Package) [20]. In order to optimize the $Cs_3Sb_2I_9$ structure, a generalized gradient approximation (GGA) with the Perdew–Burke–Ernzerhof (PBE) function was employed [21]. A projector augmented wave (PAW) was used to describe the wave function of the core region, while a linear combination of plane waves with 550 eV cut-off energy was used to describe the valence wave function. Gamma point was used to sample the reciprocal space. During geometry optimization, 10^{-5} eV and -0.1 eV/ang were used as the convergence criteria for SCF and force, respectively.

3. Results and Discussion

Figure 1a illustrates the preparation processes of the Sb-based perovskite thin film. For the W/O TU case, the films were first annealed at 70 °C for 10 min, ensuring the organic solvents could be removed completely, and then annealed in SbI_3 vapour at 250 °C for 15 min. Finally, the perovskite film was obtained. The high SbI_3 vapour pressure was considerable at 250 °C and effectively prevented the $Cs_3Sb_2I_{9-x}Cl_x$ film from losing SbI_3 [22,23]. For the W/TU case, TU decomposed during the SbI_3 vapour annealing process. Figure S1a illustrates the XRD patterns of $Cs_3Sb_2I_{9-x}Cl_x$ films containing various amounts of TU additives. The diffraction peaks at 8.7°, 17.2°, 21.0°, 25.7°, 25.9°, 29.9°, 42.7°, and 42.9° were ascribed to the (001), (002), (102), (003), (201), (022), (204), and (220) planes of the 2D $Cs_3Sb_2I_{9-x}Cl_x$ crystal phase, respectively [24]. Figure 1b shows an enlarged view of the (003) and (201) peaks in Figure S1a. In Figure 1b and Figure S1a, the relative intensities of (001), (002), and (003) peaks decrease with increasing amounts of TU. According to previous reports, the orientation of the (001), (002), and (003) planes parallel to the substrate leads to carrier transport anisotropy, which strongly limits the devices performance [10]. In addition, it can be observed in Figure 1b that the intensity of the (201) diffraction peak increases with an increasing amount of TU. The calculated data of the XRD parameters are shown in Table S1. The FWHM of the (201) plane for control, 0.1 M, 0.2 M, and 0.3 M TU additive $Cs_3Sb_2I_{9-x}Cl_x$ films was 1.516, 0.464, 0.436, and 0.454, respectively. The crystallite size of the $Cs_3Sb_2I_{9-x}Cl_x$ films was calculated by the Scherrer equation [25], the corresponding crystallite size for control, 0.1 M, 0.2 M, and 0.3 M TU was 5.621, 18.393, 19.356, and 18.795, respectively. The dislocation density of the (201) peak for control, 0.1 M, 0.2 M, and 0.3 M TU additive $Cs_3Sb_2I_{9-x}Cl_x$ films was 31.88, 2.96, 2.61, and 2.85, respectively. The lattice constants for control, 0.1 M, 0.2 M, and 0.3 M are also listed in Table S1. It was

found that the 0.2 M TU additive enhanced the crystallinity of the $Cs_3Sb_2I_{9-x}Cl_x$ films. To further understand the influence of TU on the crystal orientation of the $Cs_3Sb_2I_{9-x}Cl_x$, we calculated the peak intensity ratio (201)/(003) for the $Cs_3Sb_2I_{9-x}Cl_x$ films, and the results are shown in Figure S1b and Table S2. For the control sample, the peak intensity ratio of the (201)/(003) diffraction peaks is 0, since the (201) peak is barely detectable. The peak intensity ratios of the (201)/(003) diffraction peaks are 0.34, 2.01, and 1.25 for the 0.1 M, 0.2 M, and 0.3 M TU additives, respectively. The maximum value of (201)/(003) for the 0.2 M TU additive $Cs_3Sb_2Cl_xI_{9-x}$ films exhibits the preferred (201) growth orientation of the $Cs_3Sb_2I_{9-x}Cl_x$ crystals (Figure S1b). Figure 1c–f shows the scanning electron microscopy (SEM) images of the control, 0.1 M, 0.2 M, and 0.3 M TU additive $Cs_3Sb_2I_{9-x}Cl_x$ films. The film without TU (Figure 1c) shows a rough and irregular morphology with small grain sizes. In contrast, films with the TU additive (Figure 1d–f) exhibit a smooth and compact film with a large grain. In particular, the 0.2 M TU additive film demonstrates the largest grain sizes and high compactness. According to Lewis acid–base adduction matching rules, sulphur is a kind of soft base that can form a stable coordination with Sb^{3+}, further modulating perovskite nucleation and crystallization [26,27]. However, further increasing the addition of TU to 0.3 M results in cavities on the surface of the perovskite, which could be due to the gas generated from TU thermal decomposition ($CH_4N_2S = H_2S + CH_2N$) [19]. Meanwhile, the statistical distribution of grain sizes in the $Cs_3Sb_2I_{9-x}Cl_x$ films with the addition of different amounts of TU obtained from top-view SEM images using nano measurer software is shown in Figure 1g. Apparently, the average grain size of perovskite increases significantly after the addition of TU. It is worth noting that the 0.2 M TU additive $Cs_3Sb_2Cl_xI_{9-x}$ films show a maximum average grain size of 282.4 nm, which is much larger than that of the control film of 162.3 nm (Figure 1g). The increase in the grain sizes and reduction in the boundary areas could reduce charge carrier trapping [28]. In Figure S2a,b, the film roughness of the control and 0.2 M TU additive $Cs_3Sb_2I_{9-x}Cl_x$ films were 72.6 nm and 21.9 nm, respectively, indicating that the 0.2 M TU additive $Cs_3Sb_2I_{9-x}Cl_x$ films have small surface roughness. Figure S2c,d show the Kelvin probe force microscope (KPFM) of the control and the 0.2 M TU additive $Cs_3Sb_2I_{9-x}Cl_x$ films, respectively. The 0.2 M TU additive $Cs_3Sb_2I_{9-x}Cl_x$ films surface exhibited a higher electronic chemical potential than that of the control film, resulting from a low surface trap density and high carrier concentration [29,30]. Additionally, to further explore the dispersion of elements in the perovskite film, energy-dispersive spectroscopy (EDS) mapping was carried out to characterize the 0.2 M TU additive $Cs_3Sb_2I_{9-x}Cl_x$ films (Figure S3). As shown in Figure S3, the films demonstrate a uniform distribution of the Cs, Sb, I, and Cl elements. Meanwhile, no S was found in the film.

The XRD patterns of the control and the 0.2 M TU additive $Cs_3Sb_2I_{9-x}Cl_x$ films with different SbI_3 vapour annealing times are shown in Figure S4a,b. Figure 2a shows an enlarged view of the (003) peak in Figure S4a. As shown in Figure 2a, the (003) peak first shifted to larger angles and then to smaller angles with increasing SbI_3 vapour annealing time. The shift is especially obvious for 3 min in SbI_3 vapour annealing. The (201) diffraction peak could not be seen in Figure 2a. When the annealing time was further extended from 5 min to 10 min, no further changes in the peak position were observed. It was obvious that a large amount of chlorine first entered the $Cs_3Sb_2I_{9-x}Cl_x$ lattice, and then it was eliminated from the $Cs_3Sb_2I_{9-x}Cl_x$ lattice during SbI_3 vapour annealing due to the small ionic radius of Cl^-. Furthermore, the intensity of the (003) peak increased as the SbI_3 vapour annealing time increased, indicating the enhanced crystallinity of $Cs_3Sb_2I_{9-x}Cl_x$ films. The (003) and (201) peaks in Figure S4b are enlarged in Figure 2b. In contrast to the result shown in Figure 2a, an obvious (201) diffraction peak appears in Figure 2b. The (201) diffraction peak initially increases and then remains unchanged in the SbI_3 vapour annealed for 10 min (Figure 2b). The intensity of the (003) diffraction peak initially increased and then decreased as annealing in SbI_3 increased. These results clearly demonstrate that TU strongly affects the orientation of the $Cs_3Sb_2I_{9-x}Cl_x$ films. In the presence of TU, the intermediate phase $CsI \cdot SbI_3 \cdot SbCl_3 \cdot TU$ would be formed in the precursor solution. Figure

S5 shows Fourier-transform infrared (FTIR) spectra of the TU, CsI·SbI$_3$·SbCl$_3$·TU before SbI$_3$ vapour annealing, and CsI·SbI$_3$·SbCl$_3$·TU after SbI$_3$ vapour annealing. Figure 2c shows an enlarged view of infrared peaks in Figure S5. The peak at a wavenumber of 730 cm^{-1} corresponds to the stretching vibration of C=S in TU, which is shifted to 700 cm^{-1} for CsI·SbI$_3$·SbCl$_3$·TU before SbI$_3$ vapour annealing [31]. The shift of the C=S stretching vibration frequency was ascribed to the decrease of the bond between carbon and sulphur upon the adduct interaction of TU and CsI·SbI$_3$·SbCl$_3$ [32]. Therefore, TU was involved in the CsI·SbI$_3$·SbCl$_3$·TU formation process. After the SbI$_3$ vapour annealing, the intermediate phase changed to Cs$_3$Sb$_2$I$_{9-x}$Cl$_x$ perovskite phase, and TU was thermally decomposed, as shown in Figure 2c.
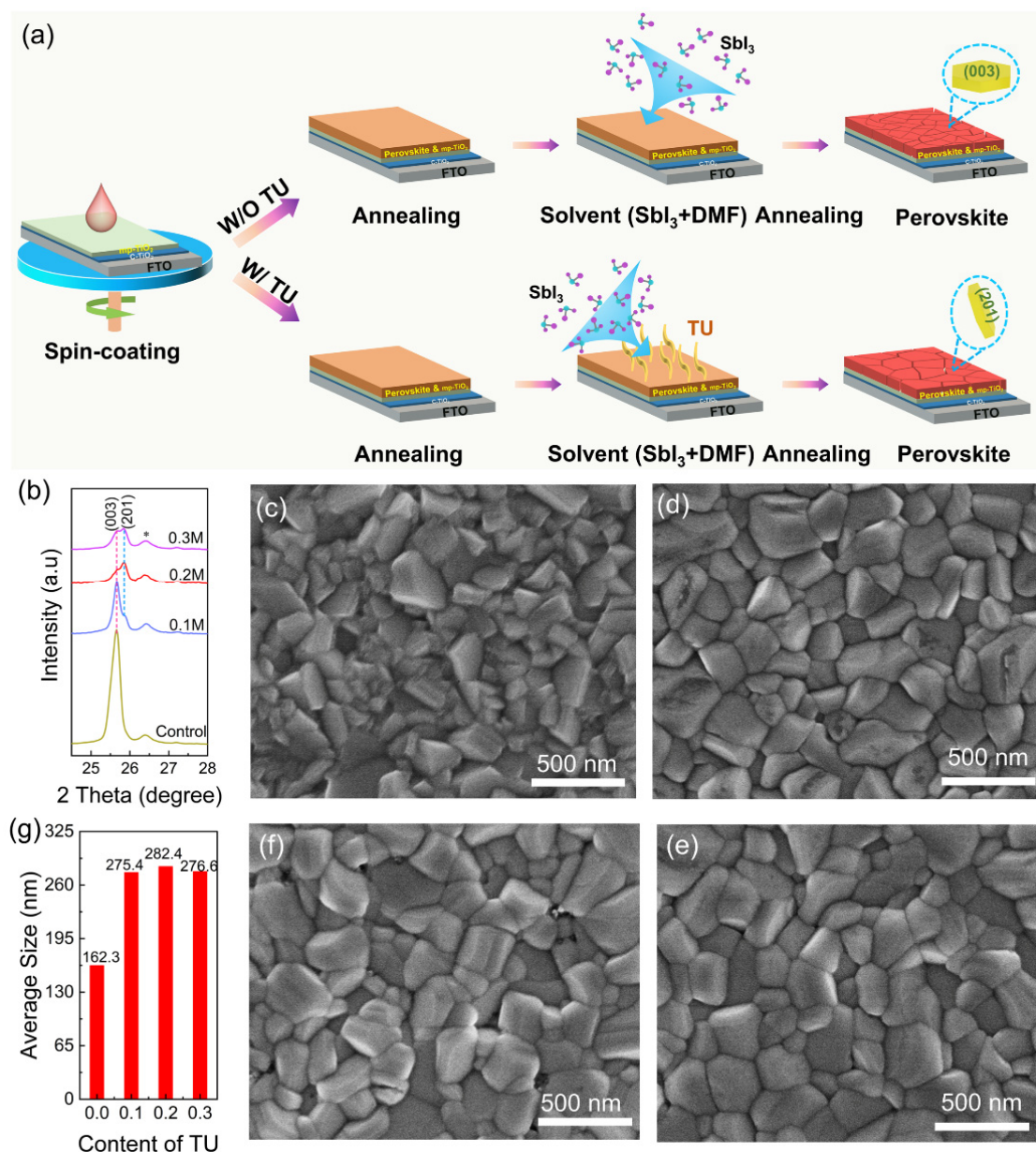

Figure 1. (**a**) Illustration of the Sb-based perovskite film fabrication procedure. (**b**) XRD patterns of the prepared Cs$_3$Sb$_2$I$_{9-x}$Cl$_x$ film with various amounts of TU. The XRD peak of "*" symbols belong to the TiO$_2$/FTO substrates. (**c–f**) SEM of the control, 0.1, 0.2 M TU, and 0.3 M additive Cs$_3$Sb$_2$I$_{9-x}$Cl$_x$ films. (**g**) The grain size statistical distribution of the control, 0.1M, 0.2M, and 0.3M TU additive Cs$_3$Sb$_2$I$_{9-x}$Cl$_x$ films.

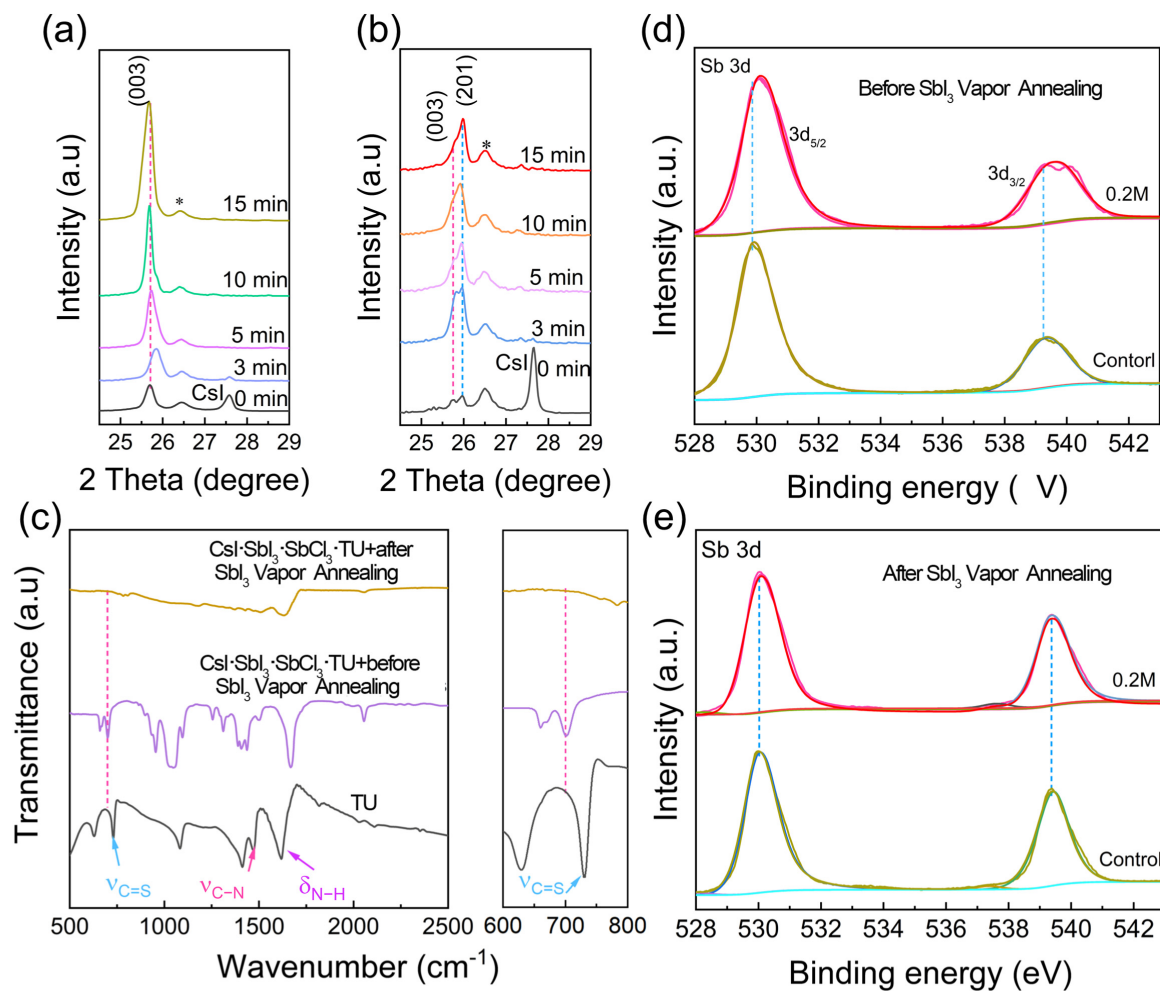**Figure 2.** XRD diffraction patterns of (**a**) the control and (**b**) 0.2 M TU additive $Cs_3Sb_2I_{9-x}Cl_x$ films under different SbI_3 vapour annealing time. The annealing time was assigned 0 min, 3 min, 5 min, 10 min, and 15 min, respectively. The XRD peak of "*" symbols belong to the TiO_2/FTO substrates. (**c**) FTIR spectra of TU, $CsI·SbI_3·SbCl_3·TU$ before SbI_3 vapour annealing, and $CsI·SbI_3·SbCl_3·TU$ after SbI_3 vapour annealing. (**d,e**) XPS for Sb 3d core level spectra in control and 0.2 M TU additive $Cs_3Sb_2Cl_xI_{9-x}$ films before and after SbI_3 vapour annealing, respectively.

To further investigate the elemental characteristics of the control and 0.2 M TU additive $Cs_3Sb_2I_{9-x}Cl_x$ films, XPS (X-ray photoelectron spectroscopy) was performed. Figure S6 shows XPS survey spectra of the 0.2 M TU additive $Cs_3Sb_2I_{9-x}Cl_x$ films before and after SbI_3 vapour annealing. It clearly indicates the presence of Cs, Sb, I, Cl, and S in the films before SbI_3 vapour annealing. Figure 2d,e shows the XPS results of Sb 3d peaks for the control and 0.2 M TU additive $Cs_3Sb_2I_{9-x}Cl_x$ films before and after SbI_3 vapour annealing. For the control and 0.2 M TU additive $Cs_3Sb_2I_{9-x}Cl_x$ films before SbI_3 vapour annealing, the Sb 3d5/2 peaks are located at 529.88 eV and 530.1 eV, respectively, which indicates a strong intermolecular interaction between Sb^{3+} and TU [24]. Moreover, as shown in Figure 2e, the Sb 3d5/2 peaks had no obvious change for the control and 0.2 M TU additive $Cs_3Sb_2I_{9-x}Cl_x$ film after SbI_3 vapour annealing. This result also indicates no residual TU in the final perovskite film. To further verify this point, we study the high-resolution S 2p and N 1s XPS spectra for the 0.2 M TU additive $Cs_3Sb_2I_{9-x}Cl_x$ films after different SbI_3 vapour annealing times. As shown in Figure S7a, the characteristic peak of N 1s located at 399.7 eV tends to decrease and disappear after 10 min of SbI_3 vapour annealing. In Figure S7b, the peak at 162.01 eV corresponds to S 2p of the TU. Meanwhile, no S 2p signals were detected

in the TU additive perovskite film after 5 min of SbI_3 vapour annealing. Therefore, we deduced that TU was removed from the perovskite film during SbI_3 vapour annealing [33].

Figure 3a,b shows the atomic structure of the optimized $Cs_3Sb_2I_8Cl$ (001) and (201) surfaces with the TU molecule. In Figure 3a,b, the TU molecule was placed on $Cs_3Sb_2I_8Cl$ (003) and (201) planes, in which the C=S groups anchor at the central Sb ion. The theoretical results based on DFT reveal that TU is adsorbed strongly on the (201) plane with an adsorption energy of −0.36 eV, which is much larger than that on the (003) plane of −0.22 eV. In addition, the large adsorption energy indicates that TU molecules interact strongly with the (201) oriented $Cs_3Sb_2I_{9-x}Cl_x$ plane. According to previous studies, the (003) plane with a lower adsorption energy with TU grows much faster than the (201) plane and eventually disappears, which agrees with the XRD results [34]. Figure 3c provides a schematic diagram of the crystallization process of the $Cs_3Sb_2I_{9-x}Cl_x$ film. For the W/O TU case, the $Cs_3Sb_2I_{9-x}Cl_x$ films crystallize rapidly during annealing. For the W/TU case, the intermediate phase $CsI·SbI_3·SbCl_3·TU$ could effectively delay the rapid nucleation during the annealing to obtain dense and smooth $Cs_3Sb_2I_{9-x}Cl_x$ films along with TU decomposition [35].

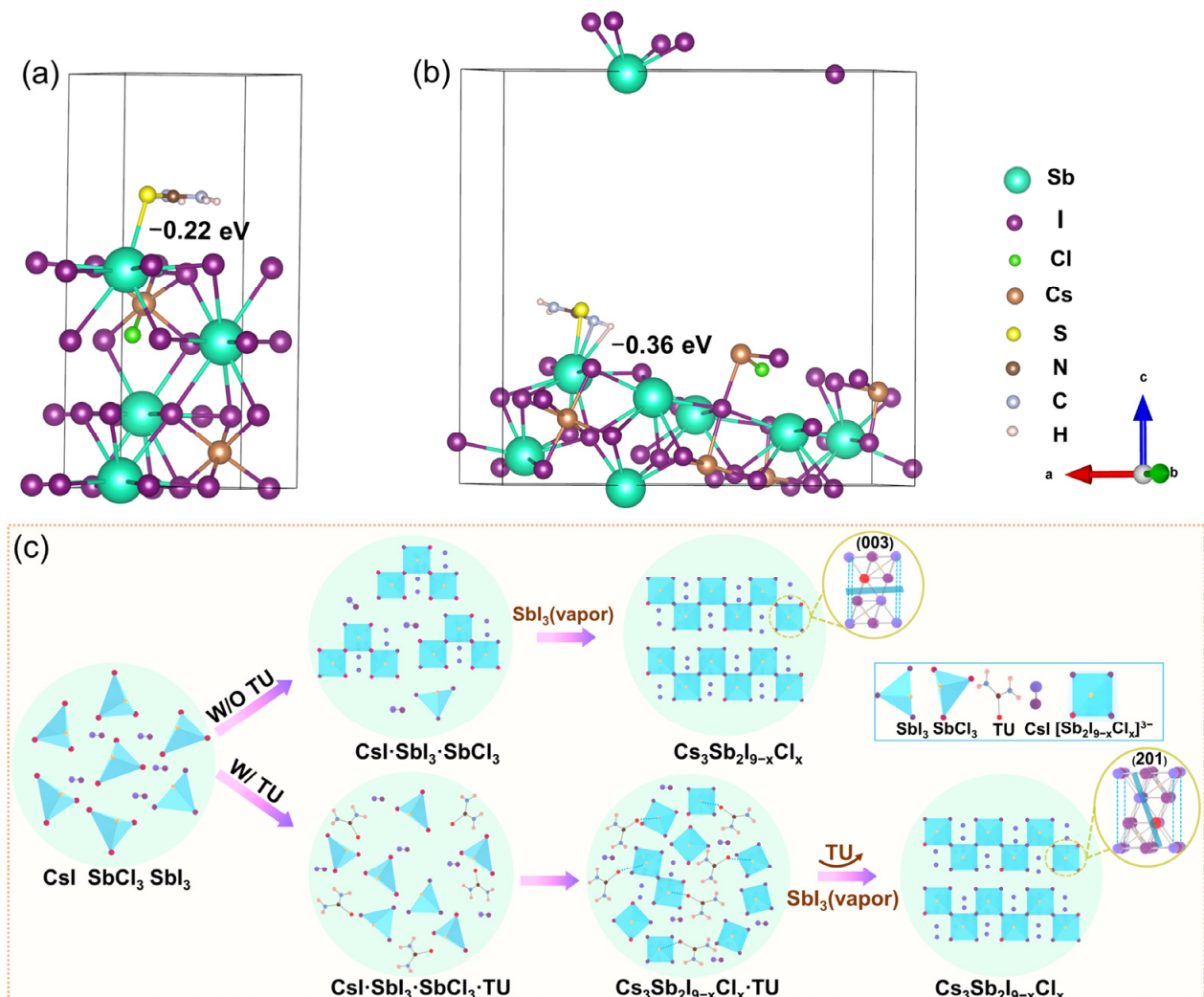**Figure 3.** Atomic structure of optimized $Cs_3Sb_2I_8Cl$ (**a**) (001) and (**b**) (201) surface with TU molecule. (**c**) Illustration of the crystallization process of $Cs_3Sb_2I_{9-x}Cl_x$ perovskite film.

Figure S8a shows the UV–vis absorption spectrum for $Cs_3Sb_2I_{9-x}Cl_x$ films containing a different content of TU additive. Tauc plots for the assessed band gap value are shown in Figure S8b. Figure S8b shows that the control and TU additive perovskite film absorption

edge were all located at 605 nm (2.05 eV), similar to previous reports [24]. Steady-state photoluminescence (PL) and time-resolved photoluminescence (TRPL) decay measurements were carried out to explore the trap states and charge recombination dynamics in control and different amounts of TU additive $Cs_3Sb_2I_{9-x}Cl_x$ films, and its structure was glass substrate/$Cs_3Sb_2I_{9-x}Cl_x$ film. As shown in Figure 4a, it is clear that the emission peaks are located at around 625 nm, conforming to the previous report [10]. The PL peak intensity of the $Cs_3Sb_2I_{9-x}Cl_x$ film shows a trend of increasing first and then decreasing with the increases of TU from 0.1 M to 0.3 M. The 0.2 M TU additive film exhibits the highest PL peak intensity, which indicates that the nonradiative recombination was suppressed [36]. When the amount of TU was 0.3 M, the PL peak intensity became weakened as a result of the increase in the nonradiative recombination and defect density. This might be caused by the presence of cavities on the 0.3 M TU additive film due to the gas generated from the thermal decomposition of TU ($CH_4N_2S = H_2S + CH_2N$) [19]. Meanwhile, the 0.3 M TU additive could lead to impurities in the film, which would increase the nonradiative recombination. Fewer traps in the $Cs_3Sb_2I_{9-x}Cl_x$ film with the 0.2 M TU additive were further confirmed by TRPL, as shown in Figure 4b and Table S3. The average decay lifetime was prolonged from 2.16 ns (control) to 15.5 ns (0.2 M TU additive), indicating that the nonradiative recombination could be reduced owing to the low defect states of large-grained $Cs_3Sb_2I_{9-x}Cl_x$ films. The TRPL results were in good agreement with the steady-state PL results. Therefore, the smooth surface, large grain size, and high crystallinity of $Cs_3Sb_2I_{9-x}Cl_x$ films played a crucial role in reducing the defects states and further suppressing the nonradiative recombination.
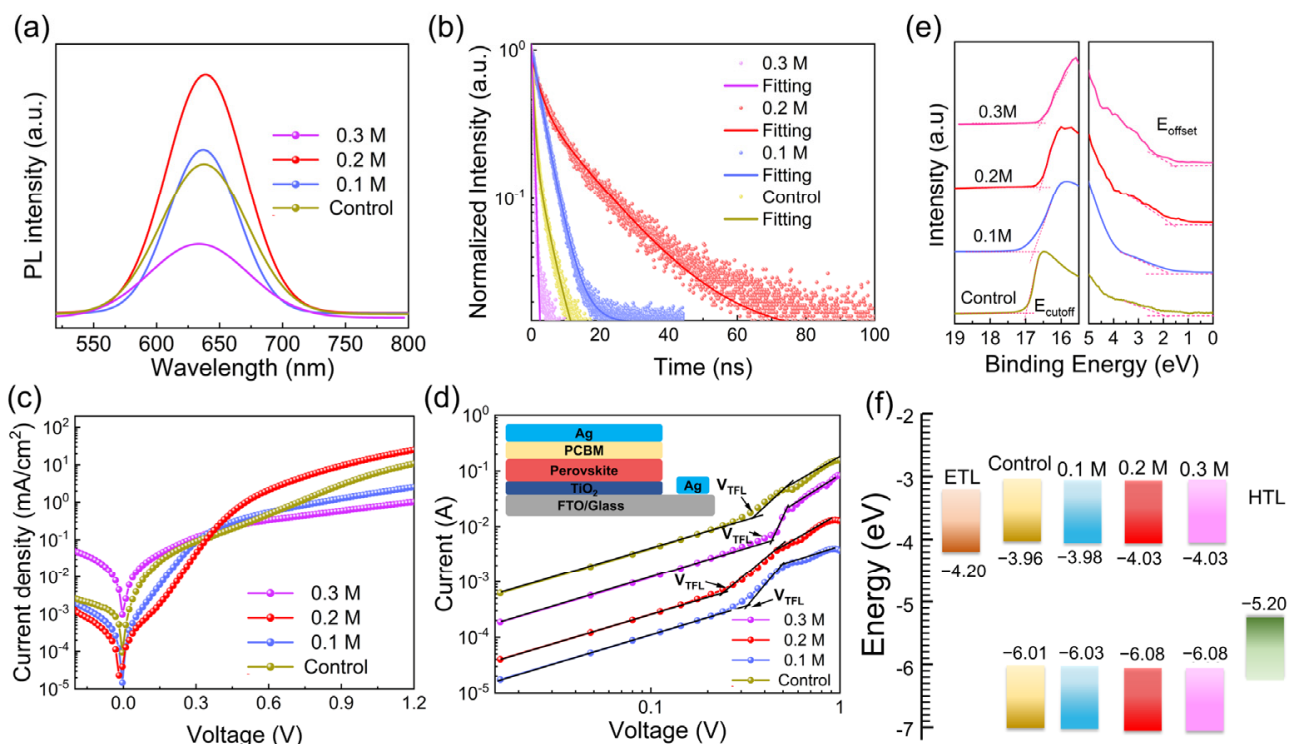

Figure 4. (**a**) Steady state PL spectra and (**b**) Time-resolved PL spectra of the control and different amounts of TU additive $Cs_3Sb_2I_{9-x}Cl_x$ perovskite films. (**c**) Dark *J–V* curves of control and TU additive $Cs_3Sb_2I_{9-x}Cl_x$ perovskite films. (**d**) Electron-only devices for measuring the trap-state density of control and TU additive $Cs_3Sb_2I_{9-x}Cl_x$ perovskite films. (**e**) UPS spectra corresponding to the valence band (VB) and cutoff regions of the control and different amounts of TU additive $Cs_3Sb_2I_{9-x}Cl_x$ perovskite films. (**f**) Energy diagrams of the control and different amounts of TU additive $Cs_3Sb_2I_{9-x}Cl_x$ perovskite films.

Moreover, to evaluate the charge transfer properties of the devices, the electron state density (N_{trap}) was calculated. We also measured *J–V* curves of devices in the dark (Figure 4c). The 0.2 M TU additive $Cs_3Sb_2I_{9-x}Cl_x$ films had a much lower leakage current than the other devices, which might be associated with the increase of grain size and reduction of defects in the film [37]. Space for charge limited current (SCLC) also was used to estimate defect properties of the devices and the results are shown in Figure 4c and Table S4. The trap state densities were calculated on the basis of the formula: [38] $N_t = 2\varepsilon_0\varepsilon V_{TFL}/qL^2$ (q is the elemental charge, ε_0 is the vacuum permittivity, ε is the relative dielectric constant and L is the thickness of the $Cs_3Sb_2I_{9-x}Cl_x$ film). For the 0.2 M TU additive $Cs_3Sb_2I_{9-x}Cl_x$ films, the lower trap-filled limit voltage (V_{TFL}) was 0.23 V for electron-only, which indicated the trap density had an impressive reduction. Ultraviolet photoelectron spectroscopy (UPS) results in Figure 4e show that the control, 0.1 M TU, 0.2 M TU, and 0.3 M TU additive $Cs_3Sb_2I_{9-x}Cl_x$ films have valence band maxima at −6.01 eV, −6.03 eV, −6.08 and −6.08 eV, respectively. Figure 4f shows a schematic energy level diagram of the materials used in the device. Figure S9 shows the band energy diagrams for the control, 0.1 M, 0.2 M and 0.3M TU additive $Cs_3Sb_2I_{9-x}Cl_x$ PSCs. The energy-level alignment of the conduction band minimum between $Cs_3Sb_2I_{9-x}Cl_x$ and TiO_2 was improved through the addition of TU into $Cs_3Sb_2I_{9-x}Cl_x$ film. The VB/CB edge of the absorber shifted downwards upon the addition of TU. These downshifts in VB/CB benefited the electric charge transport and improved the PCE [39].

The cross-sectional SEM image of the device based on a 0.2 M TU additive $Cs_3Sb_2I_{9-x}Cl_x$ perovskite film is shown in Figure 5a, which has a thickness of cp−TiO_2, mp−TiO_2, $Cs_3Sb_2I_{9-x}Cl_x$, Spiro-OMeTAD, and Au layers for 20 nm, 200 nm, and 290 nm, 90 nm, and 65 nm, respectively. Figure S10a,b show the cross-sectional SEM images of control and 0.2 M TU additive $Cs_3Sb_2I_{9-x}Cl_x$ films (290 nm), respectively. It is apparent that the 0.2 M TU additive $Cs_3Sb_2I_{9-x}Cl_x$ film grains exhibit a uniform structure from bottom to top. The uniform and dense perovskite grains will enhance the carrier transport in the device [40]. The *J–V* curves for devices fabricated with $Cs_3Sb_2I_{9-x}Cl_x$ films with different amounts of TU are presented in Figure 5b, and the specific performance parameters are shown in Table S5. In Figure 5b, as the TU content increases, the short–circuit density (J_{SC}) improves, and the 0.2 M TU additive $Cs_3Sb_2I_{9-x}Cl_x$ films devices obtain the highest efficiency of 2.22% under the 1–sun condition, which is attributed to the preferred orientation, smooth surface, and high crystallinity of perovskite films resulting in an improved carrier transport. The comparison of the efficiency with representative studies of $Cs_3Sb_2I_{9-x}Cl_x$ PSCs summarized in Table S6, which clearly illustrates that our research produces a high J_{SC} for PSCs while maintaining an excellent PCE [10,13,14,24,41]. The $Cs_3Sb_2I_{9-x}Cl_x$ films with 0.3 M TU additive exhibited a poor photoelectric performance as a result of the appearance of a pinhole in the film. The external quantum efficiency (EQE) spectrum is shown in Figure 5c. The increases of integrated J_{SC} from 5.75 mA cm^{-2} to 6.77 mA cm^{-2} upon the addition of 0.2 M TU was in accordance with the measured J_{SC} from the *J–V* plots. The data of the fabricated PSCs are counted in Figure S11. These statistical parameters clearly reveal that the 0.2 M TU additive could efficiently enhance the photovoltaic performance of the PSCs. The Nyquist plots and fitting lines measured under ambient–air dark conditions are shown in Figure 5d. The inset gives an equivalent circuit. Table S7 lists the fitting parameters. Notably, the 0.2 M TU additive $Cs_3Sb_2I_{9-x}Cl_x$ PSCs device shows the largest charge recombination resistance (R_{rec}) (178.1) compared to the control device (99.1). The series resistance of the 0.2 M TU additive of the $Cs_3Sb_2I_{9-x}Cl_x$ PSCs device exhibits a lower value (7.2 Ω) than that of control (9.4 Ω) due to the improved crystal orientation and morphology of perovskite film, demonstrating the boosting of charge transfer and the enhancing of the fill factor (FF) value. Capacitance-voltage (C−V) was carried out to explain the kinetics of the charge recombination and the increment of voltage values. The built−in potentials can be extracted in accordance with the Mott–Schottky Equation (1): [19].

$$\frac{1}{C^2} = \frac{2}{\varepsilon_0\varepsilon eA^2N_A}(V_{bi} - V) \tag{1}$$

where C is the capacitance, V is the applied voltage, V_{bi} is the built–in potential, A is the device area, ε is the relative permittivity, ε_0 is the vacuum permittivity, and N_A is the carrier concentration. As shown in Figure 5e, the V_{bi} of 0.2 M TU additive $Cs_3Sb_2I_{9-x}Cl_x$ PSCs was 0.65 V, which was higher than that of the control, 0.1 M TU additive, and 0.3 M TU additive devices 0.49 V, 0.46 V, and 0.45 V, respectively. The increasing V_{bi} benefitted the separation of the photogenerated carriers, which suppressed the electron-hole recombination and the [42]. The long-term stability of the 0.2 M TU additive $Cs_3Sb_2I_{9-x}Cl_x$ solar cells in N_2 environment conditions was observed (Figure 5f). The PCE of the optimal device retained approximately 87.69% of the initial value after 60 days.
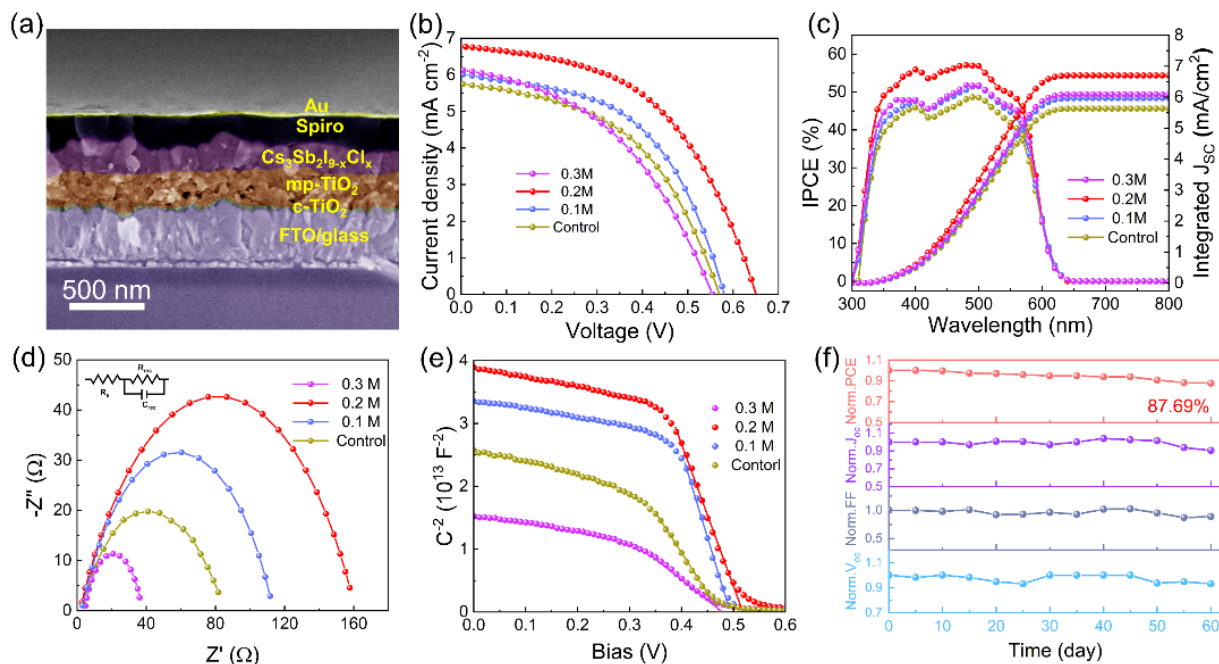

Figure 5. (**a**) Cross−section SEM image of the device. Comparison of the fabricated $Cs_3Sb_2I_{9-x}Cl_x$ films with different amounts of TU: (**b**) *J–V* curves; (**c**) EQE and integrated current density; (**d**) Nyquist plots; (**e**) Mott–Schottky curve. (**f**) Long−term stability of non−encapsulated PSCs in N_2 environment conditions.

4. Conclusions

In summary, we successfully fabricated a high-quality $Cs_3Sb_2I_{9-x}Cl_x$ film using a TU additive. TU promoted $Cs_3Sb_2I_{9-x}Cl_x$ oriented crystallization. The induced $Cs_3Sb_2I_{9-x}Cl_x$ perovskites prefered to grow in the (201) orientation, which is favourable for carrier transport. Moreover, TU also reduced the crystallization rate of $Cs_3Sb_2I_{9-x}Cl_x$ perovskites and improved the morphology of the film. The regulated crystallization orientation and morphology efficiently assisted in reducing the trap state density, restraining nonradiative recombination, and elongating the carrier lifetime. As a result, the 0.2 M TU additive devices displayed an optimal PCE of 2.22%, along with a prolonged lifetime of 87.69% for the initial PCE after 60 days in N_2 environment. This work shows a good prospect for modulating the crystallization process and orientation for high-performance $Cs_3Sb_2I_{9-x}Cl_x$ perovskite photovoltaic devices.

element distribution maps of Cs, Sb, I, Cl, and S; Figure S4. XRD diffraction patterns of (a) the control and (b) 0.2 M TU additive $Cs_3Sb_2I_{9-x}Cl_x$ films under different SbI_3 vapor annealing time. The annealing time was assigned 0, 3, 5, 10, and 15 min, respectively. The "*" symbols represent the signals of the TiO_2/FTO substrates; Figure S5. FTIR spectra of TU, $CsI \cdot SbI_3 \cdot SbCl_3 \cdot TU$ before SbI_3 vapour annealing, and $CsI \cdot SbI_3 \cdot SbCl_3 \cdot TU$ after SbI_3 vapour annealing; Figure S6. (a) XPS survey spectra of the 0.2 M TU additive $Cs_3Sb_2I_{9-x}Cl_x$ films before and after SbI_3 vapour annealing; Figure S7. (a,b) XPS results of the core-level peak for N 1s and S 2p were obtained from the 0.2 M TU additive $Cs_3Sb_2I_{9-x}Cl_x$ films under different SbI_3 vapor annealing times; Figure S8. (a) UV-visible and (b) Tauc plots of $Cs_3Sb_2I_{9-x}Cl_x$ thin films with different amounts of TU additive; Figure S9. Schematic of the band energy diagrams for the control, 0.1 M, 0.2 M and 0.3 M TU additive $Cs_3Sb_2I_{9-x}Cl_x$ PSCs; Figure S10. (a,b) Cross-sectional image of the control and 0.2 M TU additive $Cs_3Sb_2I_{9-x}Cl_x$ films; Figure S11. (a–d) Comparison of histograms of photovoltaic parameters for the perovskite solar cells based on control and 0.2M TU additive condition. (Data from 20 cells were used for the histogram); Table S1: XRD parameters of FWHM, crystallite size ($D = 0.9\lambda / \beta \cos\theta$), dislocation densities ($\delta = n/D^2$, n is a factor which is almost equal to unity for minimum dislocation density), and lattice constants for the control and different amounts of TU $Cs_3Sb_2I_{9-x}Cl_x$ films; Table S2. Intensity ratios of (201)/(003) planes of $Cs_3Sb_2I_{9-x}Cl_x$ films with different amounts of TU; Table S3. TRPL decay parameters for the control and 0.2 M TU additive $Cs_3Sb_2I_{9-x}Cl_x$ films; Table S4. The electron trap density of $Cs_3Sb_2I_{9-x}Cl_x$ films with different amounts of TU additive; Table S5. Photovoltaic parameters of the perovskite solar cells fabricated with different amounts of TU additive; Table S6. A summary of the device performance of $Cs_3Sb_2I_{9-x}Cl_x$ solar cells; Table S7 Parameters fitted from electrochemical impedance spectra of the device based on $Cs_3Sb_2I_{9-x}Cl_x$ films with different amounts of TU additive.

Author Contributions: J.L. carried out the investigation, data curation, writing original draft, writing review, and editing. Y.L. and H.H. carried out the investigation and data curation. J.X. carried out the investigation, writing review, and editing. J.Y. carried out conceptualization, validation, writing review, and editing. All authors have read and agreed to the published version of the manuscript.

Institutional Review Board Statement: Not applicable.

Informed Consent Statement: Not applicable.

Data Availability Statement: The data that support the findings of this study are available from the corresponding author upon reasonable request.

Conflicts of Interest: The authors declare no conflict of interest.

References

1. NREL. Best Research-Cell Efficiencies. Available online: https://www.nrel.gov/pv/device-performance.html (accessed on 3 December 2021).
2. Tumen-Ulzii, G.; Qin, C.; Klotz, D.; Leyden, M.R.; Wang, P.; Auffray, M.; Fujihara, T.; Matsushima, T.; Lee, J.W.; Lee, S.J. Detrimental effect of unreacted PbI_2 on the long-term stability of perovskite solar cells. *Adv. Mater.* **2020**, *32*, 1905035. [CrossRef] [PubMed]
3. Jin, Z.; Yu, B.-B.; Liao, M.; Liu, D.; Xiu, J.; Zhang, Z.; Lifshitz, E.; Tang, J.; Song, H.; He, Z. Enhanced efficiency and stability in Sn-based perovskite solar cells with secondary crystallization growth. *J. Energy Chem.* **2021**, *54*, 414–421. [CrossRef]
4. Li, Z.; Yang, M.; Li, L.; Tu, Z.; Song, L.; Ding, B.; Wang, R.; Xu, Y. Density functional theory analysis of structural and electronic properties of hexagonal hybrid perovskite $(CH_3NH_3)_3Bi_2I_9$. *Phys. B Condens. Matter* **2022**, *630*, 413695. [CrossRef]
5. Jiang, X.; Li, H.; Zhou, Q.; Wei, Q.; Wei, M.; Jiang, L.; Wang, Z.; Peng, Z.; Wang, F.; Zang, Z. One-step synthesis of $SnI_2 \cdot (DMSO)_x$ adducts for high-performance tin perovskite solar cells. *J. Am. Chem. Soc.* **2021**, *143*, 10970–10976. [CrossRef]
6. Jain, S.M.; Phuyal, D.; Davies, M.L.; Li, M.; Philippe, B.; de Castro, C.; Qiu, Z.; Kim, J.; Watson, T.; Tsoi, W.C. An effective approach of vapour assisted morphological tailoring for reducing metal defect sites in lead-free, $(CH_3NH_3)_3Bi_2I_9$ bismuth-based perovskite solar cells for improved performance and long-term stability. *Nano Energy* **2018**, *49*, 614–624. [CrossRef]
7. Yang, Y.; Liu, C.; Cai, M.; Liao, Y.; Ding, Y.; Ma, S.; Liu, X.; Guli, M.; Dai, S.; Nazeeruddin, M.K. Dimension-controlled growth of antimony-based perovskite-like halides for lead-free and semitransparent photovoltaics. *ACS. Appl. Mater. Interfaces* **2020**, *12*, 17062–17069. [CrossRef]

8. Schileo, G.; Grancini, G. Lead or no lead? Availability, toxicity, sustainability and environmental impact of lead-free perovskite solar cells. *J. Mater. Chem. C* **2021**, *9*, 67–76. [CrossRef]

9. Jiang, F.; Yang, D.; Jiang, Y.; Liu, T.; Zhao, X.; Ming, Y.; Luo, B.; Qin, F.; Fan, J.; Han, H. Chlorine-incorporation-induced formation of the layered phase for antimony-based lead-free perovskite solar cells. *J. Am. Chem. Soc.* **2018**, *140*, 1019–1027. [CrossRef]

10. Singh, A.; Lai, P.-T.; Mohapatra, A.; Chen, C.-Y.; Lin, H.-W.; Lu, Y.-J.; Chu, C.W. Panchromatic heterojunction solar cells for Pb-free all-inorganic antimony based perovskite. *Chem. Eng. J.* **2021**, *419*, 129424. [CrossRef]

11. Zhou, J.; Zhao, F.; Shen, J.; Zhou, Y.; Wu, Y.; Guo, Y.; Jiang, J.; Chu, J. Inorganic lead-free antimony-based perovskite-inspired solar cells with a carbon electrode and green anti-solvent regulation. *J. Mater. Chem.* **2021**, *9*, 15301–15308. [CrossRef]

12. Pal, J.; Manna, S.; Mondal, A.; Das, S.; Adarsh, K.; Nag, A. Colloidal Synthesis and Photophysics of $M_3Sb_2I_9$ (M = Cs and Rb) Nanocrystals: Lead-Free Perovskites. *Angew. Chem. Int. Ed.* **2017**, *56*, 14187–14191. [CrossRef] [PubMed]

13. Umar, F.; Zhang, J.; Jin, Z.; Muhammad, I.; Yang, X.; Deng, H.; Jahangeer, K.; Hu, Q.; Song, H.; Tang, J. Dimensionality Controlling of $Cs_3Sb_2I_9$ for Efficient All-Inorganic Planar Thin Film Solar Cells by HCl-Assisted Solution Method. *Adv. Opt. Mater.* **2019**, *7*, 1801368. [CrossRef]

14. Peng, Y.; Li, F.; Wang, Y.; Li, Y.; Hoye, R.L.; Feng, L.; Xia, K.; Pecunia, V. Enhanced photoconversion efficiency in cesium-antimony-halide perovskite derivatives by tuning crystallographic dimensionality. *Appl. Mater. Today* **2020**, *19*, 100637. [CrossRef]

15. Liang, P.W.; Liao, C.Y.; Chueh, C.C.; Zuo, F.; Williams, S.T.; Xin, X.K.; Lin, J.; Jen, A.K. Additive enhanced crystallization of solution-processed perovskite for highly efficient planar-heterojunction solar cells. *Adv. Mater.* **2014**, *26*, 3748–3754. [CrossRef] [PubMed]

16. Singh, A.; Najman, S.; Mohapatra, A.; Lu, Y.-J.; Hanmandlu, C.; Pao, C.-W.; Chen, Y.-F.; Lai, C.S.; Chu, C.-W. Modulating performance and stability of inorganic lead-free perovskite solar cells via lewis-pair mediation. *ACS. Appl. Mater. Interfaces* **2020**, *12*, 32649–32657. [CrossRef] [PubMed]

17. Zhao, X.; Liu, T.; Kaplan, A.B.; Yao, C.; Loo, Y.-L. Accessing highly oriented two-dimensional perovskite films via solvent-vapor annealing for efficient and stable solar cells. *Nano Lett.* **2020**, *20*, 8880–8889. [CrossRef]

18. Donnay, J.D.H.; Harker, D. A new law of crystal morphology extending the law of Bravais. *Am. Mineral. J. Earth Planet. Mater.* **1937**, *22*, 446–467.

19. Li, J.; Liu, X.; Yao, J. The enhanced photovoltaic performance of Sb_2S_3 solar cells by thermal decomposition of antimony ethyl xanthate with thiourea doping. *Energy Technol.* **2020**, *8*, 1900841. [CrossRef]

20. Kresse, G.; Furthmüller, J. Efficient iterative schemes for ab initio total-energy calculations using a plane-wave basis set. *Phys. Rev. B* **1996**, *54*, 11169. [CrossRef]

21. Perdew, J.P.; Burke, K.; Ernzerhof, M. Generalized gradient approximation made simple. *Rev. Lett.* **1996**, *77*, 3865. [CrossRef]

22. Gregory, N.W. Equilibrium vapor concentrations in the antimony+ iodine system. Molar absorptivities of antimony (III) iodide vapor. *J. Chem. Eng. Data* **1996**, *41*, 107–112. [CrossRef]

23. Singh, A.; Boopathi, K.M.; Mohapatra, A.; Chen, Y.F.; Li, G.; Chu, C.W. Photovoltaic performance of vapor-assisted solution-processed layer polymorph of $Cs_3Sb_2I_9$. *ACS. Appl. Mater. Interfaces* **2018**, *10*, 2566–2573. [CrossRef] [PubMed]

24. Paul, G.; Pal, A.J.; Larson, B.W. Structure, Morphology, and Photovoltaic Implications of Halide Alloying in Lead-Free $Cs_3Sb_2Cl_xI_{9-x}$ 2D-Layered Perovskites. *Sol. RRL* **2021**, *5*, 2000422. [CrossRef]

25. Chelvanathan, P.; Yusoff, Y.; Haque, F.; Akhtaruzzaman, M.; Alam, M.; Alothman, Z.; Rashid, M.; Sopian, K.; Amin, N. Growth and characterization of RF-sputtered ZnS thin film deposited at various substrate temperatures for photovoltaic application. *Appl. Surf. Sci.* **2015**, *334*, 138–144. [CrossRef]

26. Patil, J.V.; Mali, S.S.; Hong, C.K. A thiourea additive-based quadruple cation lead halide perovskite with an ultra-large grain size for efficient perovskite solar cells. *Nanoscale* **2019**, *11*, 21824–21833. [CrossRef]

27. Li, X.; He, B.; Gong, Z.; Zhu, J.; Zhang, W.; Chen, H.; Duan, Y.; Tang, Q. Compositional engineering of Chloride Ion-Doped $CsPbBr_3$ halides for highly efficient and stable all-inorganic perovskite solar cells. *Sol. RRL* **2020**, *4*, 2000362. [CrossRef]

28. Liu, Z.; Liu, D.; Chen, H.; Ji, L.; Zheng, H.; Gu, Y.; Wang, F.; Chen, Z.; Li, S. Enhanced Crystallinity of Triple-Cation Perovskite Film via Doping NH_4SCN. *Nanoscale Res. Lett.* **2019**, *14*, 304. [CrossRef]

29. Liang, L.; Luo, H.; Hu, J.; Li, H.; Gao, P. Efficient Perovskite Solar Cells by Reducing Interface-Mediated Recombination: A Bulky Amine Approach. *Adv. Energy Mater.* **2020**, *10*, 2000197. [CrossRef]

30. Wang, R.; Xue, J.; Wang, K.-L.; Wang, Z.-K.; Luo, Y.; Fenning, D.; Xu, G.; Nuryyeva, S.; Huang, T.; Zhao, Y. Constructive molecular conFigureurations for surface-defect passivation of perovskite photovoltaics. *Science* **2019**, *366*, 1509–1513. [CrossRef]

31. Tiwari, D.; Fermin, D.J.; Chaudhuri, T.; Ray, A. Solution processed bismuth ferrite thin films for all-oxide solar photovoltaics. *J. Phys. Chem. C* **2015**, *119*, 5872–5877. [CrossRef]

32. Jeon, N.J.; Noh, J.H.; Kim, Y.C.; Yang, W.S.; Ryu, S.; Seok, S.I. Solvent engineering for high-performance inorganic–organic hybrid perovskite solar cells. *Nat. Mater.* **2014**, *13*, 897–903. [CrossRef] [PubMed]

33. Xu, C.; Zhang, Z.; Zhang, S.; Si, H.; Ma, S.; Fan, W.; Xiong, Z.; Liao, Q.; Sattar, A.; Kang, Z. Manipulation of Perovskite Crystallization Kinetics via Lewis Base Additives. *Adv. Funct. Mater.* **2021**, *31*, 2009425. [CrossRef]

34. Gibbs, J.W. On the equilibrium of heterogeneous substances. *Am. J. Sci.* **1879**, *3*, 441–458. [CrossRef]

35. Chen, S.; Xiao, X.; Chen, B.; Kelly, L.L.; Zhao, J.; Lin, Y.; Toney, M.F.; Huang, J.S. Crystallization in one-step solution deposition of perovskite films: Upward or downward? *Sci. Adv.* **2021**, *7*, eabb2412. [CrossRef]

36. Chen, W.; Wu, Y.; Yue, Y.; Liu, J.; Zhang, W.; Yang, X.; Chen, H.; Bi, E.; Ashraful, I.; Grätzel, M. Efficient and stable large-area perovskite solar cells with inorganic charge extraction layers. *Science* **2015**, *350*, 944–948. [CrossRef]

37. Cao, K.; Cheng, Y.; Chen, J.; Huang, Y.; Ge, M.; Qian, J.; Liu, L.; Feng, J.; Huang, W. Regulated Crystallization of FASnI$_3$ Films through Seeded Growth Process for Efficient Tin Perovskite Solar Cells. *ACS Appl. Mater. Interfaces* **2020**, *12*, 41454–41463. [CrossRef] [PubMed]

38. Bube, R.H. Trap density determination by space-charge-limited currents. *J. Appl. Phys.* **1962**, *33*, 1733–1737K. [CrossRef]

39. Wang, Y.; Dar, M.I.; Ono, L.K.; Zhang, T.; Kan, M.; Li, Y.; Zhang, L.; Wang, X.; Yang, Y.; Gao, X. Thermodynamically stabilized β-CsPbI$_3$–based perovskite solar cells with efficiencies > 18%. *Science* **2019**, *365*, 591–595. [CrossRef]

40. You, P.; Tang, G.; Cao, J.; Shen, D.; Ng, T.-W.; Hawash, Z.; Wang, N.; Liu, C.-K.; Lu, W.; Tai, Q.; et al. Applications, 2D materials for conducting holes from grain boundaries in perovskite solar cells. *Light Sci. Appl.* **2021**, *10*, 68. [CrossRef]

41. Hiltunen, A.; Lamminen, N.; Salonen, H.; Liu, M.; Vivo, P. Efficiency improvement for perovskite-inspired Cs$_3$Sb$_2$I$_9$ solar cells using P3HT as the hole transport material. *Sustain. Energy Fuels* **2022**, *6*, 217–222. [CrossRef]

42. Bai, D.; Zhang, J.; Jin, Z.; Bian, H.; Wang, K.; Wang, H.; Liang, L.; Wang, Q.; Liu, S.F. Interstitial Mn^{2+}-driven high-aspect-ratio grain growth for low-trap-density microcrystalline films for record efficiency CsPbI$_2$Br solar cells. *ACS Energy Lett.* **2018**, *3*, 970–978. [CrossRef]